

## PDF hosted at the Radboud Repository of the Radboud University Nijmegen

The following full text is a publisher's version.

For additional information about this publication click this link.

<http://hdl.handle.net/2066/32489>

Please be advised that this information was generated on 2018-07-07 and may be subject to change.

# Experimental and theoretical investigation of the $A\ ^3\Pi-X\ ^3\Sigma^-$ transition of NH/D–Ne

Galina Kerenskaya,<sup>a</sup> Udo Schnupf,<sup>a</sup> Michael C. Heaven,\*<sup>a</sup> Ad van der Avoird<sup>b</sup> and Gerrit C. Groenenboom<sup>b</sup>

<sup>a</sup> Department of Chemistry, Emory University, Atlanta, GA 30322, USA.

E-mail: heaven@euch4e.chem.emory.edu; Fax: 404 727 6586

<sup>b</sup> Institute of Theoretical Chemistry, NSRIM, University of Nijmegen, Toernooiveld 1, 6525 ED Nijmegen, The Netherlands

Received 1st October 2004, Accepted 24th November 2004

First published as an Advance Article on the web 6th January 2005

A study of NH/D–Ne was undertaken to investigate the structure of this complex and examine the ability of high-level theoretical methods to predict its properties. The  $A\ ^3\Pi-X\ ^3\Sigma^-$  transition was characterized using laser induced fluorescence measurements. Results from theoretical calculations were used to guide the interpretation of the spectra. Two-dimensional potential energy surfaces were calculated using second-order multireference perturbation theory with large correlation consistent basis sets. The potential energy surfaces were used to predict the ro-vibronic structure of the A–X system. Calculated ro-vibronic energy level patterns could be recognized in the spectra but quantitative discrepancies were found. These discrepancies are attributed to incomplete recovery of the dynamical correlation energy.

## Introduction

The interactions between triplet states of the NH radical and rare gas atoms have been the subject of several experimental and theoretical studies.<sup>1–12</sup> These systems provide convenient and tractable models for investigating the collision dynamics associated with  $^3\Sigma$  and  $^3\Pi$  states. Theoretical treatments of the dynamics using *ab initio* methods provide a rigorous test of the current capabilities for computing long-range forces for open-shell systems.<sup>3,7,13</sup> Recently, additional interest in the low temperature dynamics of  $\text{NH}(X\ ^3\Sigma^-) + \text{Rg}$  collisions has been stimulated by recognition that NH(X) could be cooled to ultra-low temperatures and trapped.<sup>8,10,14</sup>

Experimental studies of the inelastic collisions of NH(X) with He,<sup>5</sup> Ne<sup>4</sup> and Ar<sup>6</sup> have been carried out. It was found that rotational state changing collisions exhibited a propensity for conservation of the fine structure component. For He and Ne, Rinnenthal and Gericke<sup>4,5</sup> noted that collisions that changed the fine structure component, but not the rotational angular momentum, were most effective while transitions that changed the rotational angular momentum showed a propensity for conservation of the fine structure component. These results were consistent with semi-empirical models for  $^3\Sigma$  energy transfer, but comparisons with the results from rigorous scattering calculations have not been reported. High-quality potential energy surfaces have been calculated for NH(X)–He by Krems *et al.*<sup>10</sup> and Cybulski *et al.*<sup>8</sup> and for NH(X)–Ar by Jansen and Hess<sup>12</sup> and Kendall *et al.*<sup>11</sup> Prior to the present study, calculations for the NH(X) + Ne potential had not been published.

As it is technically easier to observe ro-vibronic energy transfer in excited states (where thermal populations are negligible), collisions between NH( $A\ ^3\Pi$ ) and the rare gases He<sup>13,15</sup> and Ar<sup>1</sup> have been examined in greater detail. Energy transfer induced by collisions with He exhibited propensities for fine structure and lambda doublet component population that were indicative of an intermediate Hund's coupling case for the low rotational levels and the case 'b' characteristics of

the higher rotational levels. Transfer between the  $\Omega = 1$  and 2 spin-orbit components, which is forbidden in the case 'a' limit, was observed for the lowest rotational levels. The experimental trends were accurately reflected in close-coupled calculations<sup>13</sup> that employed the NH(A)–He *ab initio* potential energy surfaces of Jonas and Staemmler.<sup>9</sup> A preference for the  $\Pi(A')$  lambda doublet component in downward rotational energy transfer was shown to be a consequence of the  $A''$  potential energy surface being more repulsive than the  $A'$  surface.<sup>13</sup>

Energy transfer induced by collisions with Ar was mostly governed by the tendency to minimize the change in the rotational angular momentum. Transfer between  $\Omega$  components was found to be facile, with no lambda doublet preference.<sup>1</sup>

Studies of collisional energy transfer typically provide information concerning the repulsive region of the intermolecular potential. The long-range attractive components of the potentials may be probed by examining low energy collisions and the bound levels of van der Waals wells. Bound state energies have been predicted for both NH(X)–He<sup>8</sup> and NH(X)–Ar.<sup>11</sup> The work on NH(X)–He was carried out in support of proposed cooling and trapping experiments. Cybulski *et al.*<sup>8</sup> used an *ab initio* potential energy surface to predict the cross sections for elastic vs. Zeeman state changing collisions. The van der Waals well in this potential was deep enough to support a bound zero-point level ( $D_0 = 4.4\ \text{cm}^{-1}$ ). The existence of this bound state has been confirmed recently as the NH(X)–He van der Waals complex was detected using laser excitation of the A–X transition.<sup>7</sup> NH–Ar and NH–Ne complexes in singlet states have been studied by observing bands associated with the NH  $c\ ^1\Pi-a\ ^1\Delta$  transition.<sup>16,17</sup> The spectra obtained in these experiments were congested and particularly difficult to analyze. In both instances high-level theoretical calculations were used to guide the assignment process. *Ab initio* potentials for the singlet states of NH–Ar<sup>16</sup> and NH–Ne<sup>17</sup> were sufficiently accurate to reproduce the qualitative features of the spectra, but systematic errors were revealed by quantitative comparisons. The surfaces for both

the *a* and *c* states of NH–Ar were found to be too shallow and the equilibrium bond length for the *c* state was too long. For NH–Ne the *a* state potentials yielded the correct dissociation energy, but errors in the anisotropy of the surfaces were evident. The *c* state potentials were too shallow and, contrary to the usual trend, the equilibrium bond length was too short.

In the present study we have examined the  $A^3\Pi-X^3\Sigma^-$  band system of NH–Ne. This work is complementary to our earlier investigation of the *c*–*a* transition.<sup>17</sup> Comparisons of the intermolecular potential energy surfaces for the states are of interest as a  $^1\Delta$  and  $X^3\Sigma^-$  are derived from the lowest energy electronic configuration of NH, while *c*  $^1\Pi$  and  $A^3\Pi$  are derived from the first excited configuration. Theoretical calculations for the triplet states, performed using the same level of theory as our previous study of the singlet states, are presented here. Rotationally resolved spectra were recorded for the A–X bands of both NH–Ne and ND–Ne. The theoretical calculations were used to guide the assignment of these spectra and the accuracy of the potentials was assessed in the process. The A–X spectra were found to be easier to interpret than the *c*–*a* spectra, mostly due to the simple ro-vibronic structure of the ground state.

Few complexes involving radicals in  $^3\Pi$  states have been examined to date. The properties of CO( $a^3\Pi$ )–He have been computed,<sup>18,19</sup> but there are no experimental data for this system. Our recent study of NH(A)–He appears to be the first observation of a  $^3\Pi$  complex.<sup>7</sup> For the heavier and more tightly bound NH(A)–Ne complex, we see a larger number of bound states, which facilitates evaluation of the theoretical models. We find that the essential features of the vibronic structure of NH/D(A)–Ne are reproduced using *ab initio* potential energy surfaces with the Hamiltonian operators of Alexander<sup>20</sup> and Zeimen *et al.*<sup>18</sup>

Spin-orbit predissociation of NH(A)–Ne was observed for the  $\Omega = 1$  and 0 manifolds. This corresponds to the half-collision analog of fine-structure changing collisions. Observation of  $\Omega = 1 \rightarrow 2$  predissociation shows that all levels of NH(A)–Ne depart from the Hund's case 'a' limit.

## Experimental details

NH/D–Ne complexes were formed in a free-jet expansion and detected by laser-induced fluorescence (LIF). The apparatus used for this work has been described previously.<sup>21</sup> NH/D radicals were produced by 193 nm multi-photon dissociation of  $\text{NH}_3$  or  $\text{ND}_3$ . A carrier gas mixture of Ne (70%) and He (30%) with 0.04%  $\text{NH}_3$  or  $\text{ND}_3$  was used to drive the expansion. The gas mixture was expanded through the 0.7 mm orifice of a pulsed valve (General Valve, Series 9), operated at a repetition rate of 10 Hz with a pulse duration of 1.3 ms. Optimal formation of NH(X)–Ne was observed using a source pressure of 13 atm.

The beam from a pulsed tunable dye laser crossed the expansion approximately 7 mm from the nozzle orifice. Wavelengths in the range 334–337 nm were obtained using the dye *p*-terphenyl. Frequency doubling of the laser was used to generate light in the 303–306 nm range. LIF was dispersed by a 0.25 m monochromator and detected by a photomultiplier. In these experiments the monochromator was used primarily as a band-pass filter. A slit width of 6 mm, corresponding to a band-pass of 12 nm, was used. Typically the monochromator was set to monitor the NH/D A–X 0–0 or 1–1 emission bands (near 336 nm).

NH/D–Ne A–X spectra were recorded at low ( $0.5\text{ cm}^{-1}$  linewidth) and medium ( $0.1\text{ cm}^{-1}$ ) resolution. The lines of the monomer were used to calibrate the spectra using the line positions from Brazier *et al.*<sup>22</sup> for NH and the data of Bollmark *et al.*<sup>23</sup> for ND.

## Notation

Before describing the experimental results it is helpful to define the system of notation that will be used to discuss the spectra. We will adopt the convention of using lower case quantum number labels for properties of the monomer and upper case quantities for properties of the entire complex.<sup>24</sup> The  $X^3\Sigma^-$  state of NH is characterized by the quantum numbers *n* and *j*, which represent the rotational angular momentum and the total angular momentum (exclusive of nuclear spin), respectively. The  $A^3\Pi$  state is also characterized by *j*. The projection of the total angular momentum on the diatomic axis (denoted by  $\omega$ ) is a useful quantum label, but, as NH(A) is not close to the Hund's case 'a' limit, it is not a conserved quantity. For the lowest rotational levels it is reasonable to associate the  $F_1$ ,  $F_2$ , and  $F_3$  spin-orbit components with  $\omega = 2, 1$  and 0. For the complex *L* is used to designate the angular momentum for end-over-end rotation. This is a good quantum number for NH/D(X)–Ne which closely approximates to the case 'B' coupling scheme of Dubernet *et al.*<sup>24</sup> The total angular momentum of the complex in both the X and A states is given by the vector sum  $\mathbf{J} = \mathbf{j} + \mathbf{L}$ . The projection of both *j* and *J* on the intermolecular axis (Jacobi coordinate *R*), designated by the unsigned quantum number *P*, is also a reasonably well defined property of NH/D(A)–Ne.

## Experimental results and data analysis

Ro-vibronic bands of the NH/D–Ne complex were observed in association with the monomer A–X 0–0 and 1–0 transitions. Fig. 1 shows a low-resolution spectrum taken in the region of the 0–0 transition. The structure observed for the 1–0 transition was closely similar. The three strongest monomer lines in Fig. 1 correspond to transitions from the  $n'' = 0, j'' = 1$  level to the lowest energy levels of the spin-orbit components of  $A^3\Pi$  ( $\omega' = j' = 2, 1$  and 0). Features of the complex were observed near to each of these lines. The lower energy complex bands exhibited resolvable rotational structure. Examples of resolved bands are shown in Figs. 2–4, which correspond to the bands labeled A, B and C in Fig. 1. Similar structures were observed for ND–Ne, and Fig. 5 shows an example of the rotational structure for the heavier isotope. Complex features observed at energies higher than the monomer  $Q_{21}(1)$  line were broadened by predissociation and could not be resolved.

The rotational structures of the NH/D–Ne bands were analyzed by treating the complex as a rigid pseudo-diatomic

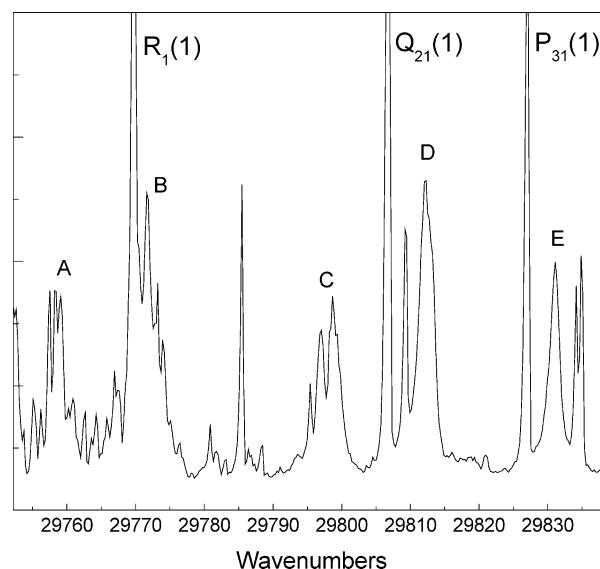


**Fig. 1** Low resolution spectrum of NH and NH–Ne taken in the region of the A–X 0–0 band. The features of the complex are marked with labels A–E.

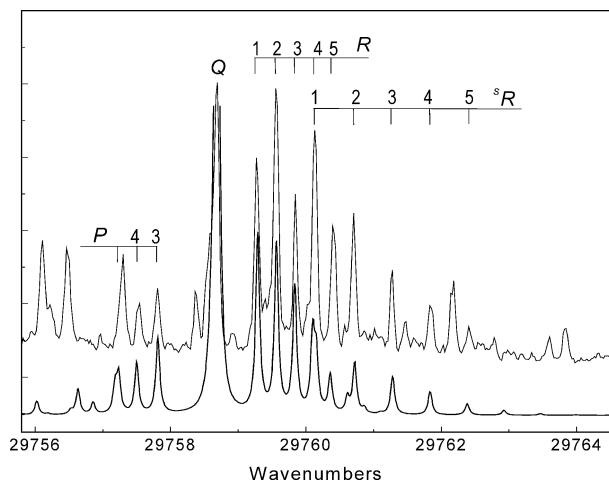


**Fig. 2** Rotationally resolved spectrum for the NH-Ne band marked as 'A' in Fig. 1. The upper trace shows the experimental result. The lower trace is a rigid rotor simulation. See text for details.

rotor. The rotational energy levels of the upper and lower states were represented by  $E'_{\text{Rot}} = B'J'(J' + 1)$  and  $E''_{\text{Rot}} = B''L''(L'' + 1)$ . The latter expression was used as the spin-splitting in the ground state could not be resolved, so the levels are characterized by the end-over-end rotational quantum number  $L$ . For the A-state the electronic angular momentum is coupled to the diatomic and intermolecular axes. Consequently the  $J$  quantum number is used to represent the rovibronic levels of NH(A)-Ne. Preliminary assignments of the rotational structures were made using the traditional combination differences approach. Note that the  $P$  quantum number of the upper state could be uniquely determined when the first line of the P-branch could be identified. Once the line assignments had been established, least squares fitting to the line positions was used to refine the rotational constants and define the band origins. To check the quality of each fit and assignment of the band type, the constants were used to simulate the bands. Relative line intensities were derived by assuming a Boltzmann rotational distribution and Honl-London linestrength factors (with  $P$  defining the body-fixed projection of the angular momentum). The latter approximation is crude, given that  $P$  is not well defined for the ground state. However, with some

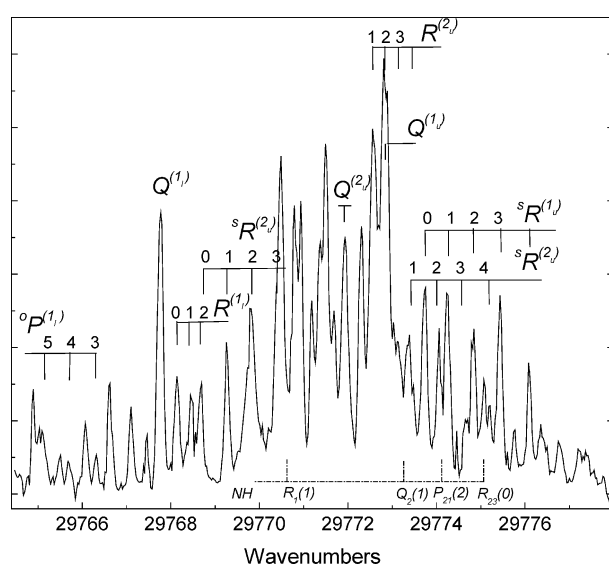


**Fig. 3** Rotationally resolved spectrum of the cluster of NH-Ne bands marked as 'B' in Fig. 1. The lines of the monomer have been subtracted from this spectrum. The broken grid below the spectrum indicates the positions where the strongest monomer lines occur. The grids above the spectrum indicate partial rotational assignments for the NH-Ne bands.

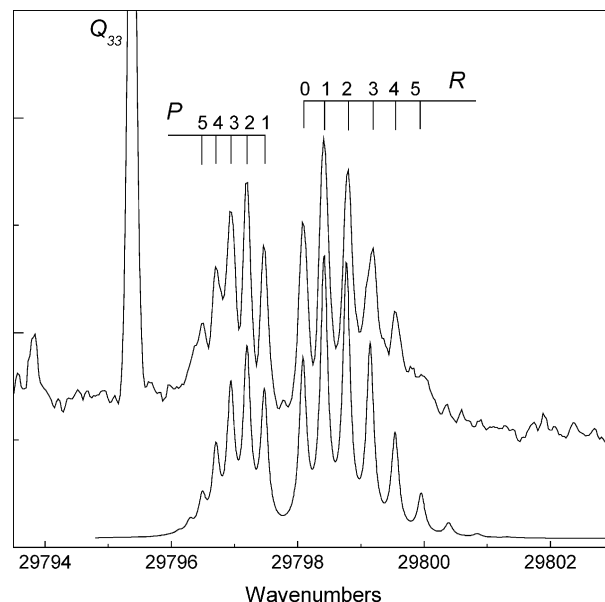


**Fig. 4** Rotationally resolved spectrum of the NH-Ne band marked as 'C' in Fig. 1. Note the small increase in the linewidth that occurs with increasing  $J$  in the experimental data. For the simulated spectrum (lower trace) the linewidth was held at the instrumental value.

additional scaling this approach yielded helpful simulations. A simulation of the lowest energy band for NH-Ne is shown alongside the experimental spectrum in Fig. 2. This calculation was performed with  $P' = 2$  and  $P'' = 1$ . The  $^{\text{O}}\text{P}$ - and  $^{\text{S}}\text{R}$ -branch intensities were scaled relative to the other branches in the band. The rotational temperature derived from this simulation (2 K) was in good agreement with the temperature observed for bands of the  $c^1\Pi - a^1\Delta$  transition, which were recorded under the same conditions.<sup>17</sup> The complex features observed near the monomer  $R_1(1)$  transition had sharp rotational structure, but the level of congestion indicated the presence of several overlapping bands. Fig. 3 shows the relevant spectral region for NH-Ne. The monomer lines were removed from this scan by subtracting a spectrum that was recorded under conditions where very little of the complex was formed. Transitions to

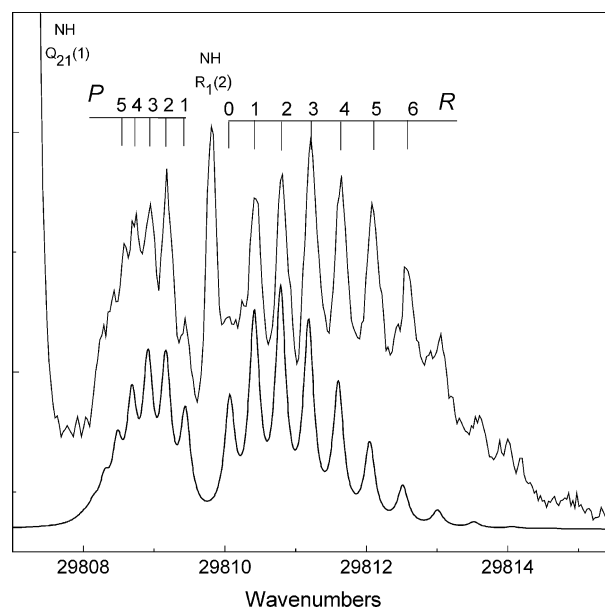


**Fig. 5** Rotationally resolved spectrum for ND-Ne. This band is the isotopic equivalent of the band shown in Fig. 4. Note that line near the center of the complex band is NH  $R_1(2)$ . Despite the use of  $\text{ND}_3$  in these measurements, NH lines were always present due to desorption of  $\text{NH}_3$  from the walls of the gas supply line.

three  $P' > 0$  states were identified in this group. The congestion was such that we were unable to identify the first rotational lines in these bands without ambiguity. Consequently the  $P'$  assignments indicated in Fig. 3 (by superscripts on the rotational branch labels) were made using the theoretical calculations described below.

For both NH–Ne and ND–Ne the highest energy bands with resolvable structure exhibited the characteristics of a  $P' = 0 \leftarrow P'' = 0$  transition at the present level of resolution. Simulations of these bands are shown in Figs. 4 and 5. The linewidths of the spectra shown in Figs. 4 and 5 were slightly greater than the instrumental linewidth, and increased with rotational excitation. Origins, rotational constants, and  $P'$  assignments for the A–X bands of NH/D–Ne are collected in Table 1. Band centers are given for features that could not be resolved due to homogeneous line broadening.

The energy ranges spanned by the resolvable bands of NH/D(A,  $\nu = 0$ )–Ne establish lower bounds for the dissociation energies. The highest energy features ( $P' = 0^-$ ) were homogeneously broadened, indicating that these levels lie above the NH/D(A  $^3\Pi_2, j = 2$ ) + Ne dissociation asymptote. Furthermore, the relatively large rotational constants for these states indicate that they are derived from NH/D(A  $^3\Pi_1, j = 1$ ) + Ne. The rotational structures of the bands below  $P' = 0^-$  were sharp, bracketing the dissociation energy in the range of  $14.6 < D'_0 < 40.4 \text{ cm}^{-1}$  for NH(A)–Ne and  $17 < D'_0 < 42 \text{ cm}^{-1}$  for ND(A)–Ne. Combined with the red-shift of the origin band relative to the monomer  $R_1(1)$  line ( $12.4 \text{ cm}^{-1}$  for NH–Ne) this defines a range for the dissociation energy for NH(X)–Ne of  $2.2 < D'_0 < 28.0 \text{ cm}^{-1}$ .

## Theoretical investigation of the NH/D–Ne A $^3\Pi$ –X $^3\Sigma^-$ transition

### Potential energy surfaces

The methods used to calculate the potential energy surfaces for singlet states of NH–Ne were described in ref. 17. The same approach has been used to obtain surfaces for the X  $^3\Sigma^-$  and A  $^3\Pi$  states. Initial test calculations were performed using three correlation methods, CASPT2, CASPT3 and MRCI (Davidson corrected) to determine the most suitable correlation method and basis set size.

All electronic structure calculations were performed using the MOLPRO 2002 suite of programs.<sup>25</sup> The dominant electronic configurations for the NH X and A states are  $(1\sigma)^2(2\sigma)^2(3\sigma)^2(1\pi)^2$  and  $(1\sigma)^2(2\sigma)^2(3\sigma)(1\pi)^3$ . The active space

was constructed by distributing the four valence electrons among the  $(3\sigma)(1\pi)(4\sigma)$  orbitals (CAS(4,4)). Dunning's<sup>26</sup> correlation consistent basis sets were used in all calculations. Basis sets ranging in size from aug-cc-pvdz (augmented – correlation consistent – polarized valence double zeta) to aug-cc-av6z were investigated. In the following just the last four letters of the abbreviation are used to designate the basis set. To reduce the computational expense the particular basis sets were truncated to spdf functions for N and Ne, and spd for H. Jacobi coordinates were used throughout this study, with the N–H bond length frozen at  $r = 1.9583 \text{ au}$ . The Jacobi angle was chosen such that  $\theta = 0^\circ$  corresponded to linear NH–Ne. In geometrical configurations in which the NH–Ne complex has  $C_s$  symmetry the X  $^3\Sigma^-$  ground state correlates with the lowest  $^3A''$  state which has the electronic configuration  $(1a')^2(2a')^2(3a')^2(4a')^1(1a'')^1$ . Here  $1a'$ ,  $2a'$ , and  $3a'$  are the occupied  $\sigma$  orbitals of NH, while  $4a'$  and  $1a''$  are the two components of the  $1\pi$ -orbital. In  $C_s$  symmetry the A  $^3\Pi$  state splits into two components,  $A'$  and  $A''$  with the electronic configurations  $(1a')^2(2a')^2(3a')^1(4a')^1(1a'')^2$  and  $(1a')^2(2a')^2(3a')^1(4a')^2(1a'')^1$ , respectively.

Results from the test calculations are summarized in Table 2. CASPT2, CASPT3 and MRCI predicted the equilibrium structure to be linear NH–Ne for both the X and A states. Hence Table 2 lists just the well depths and equilibrium distances for these calculations. As in the previous study of the singlet states it was found that the CASPT2 method with the av6z basis set, without the counterpoise correction, provided the best compromise between accuracy and computation time for NH(A)–Ne. Inclusion of the BSSE correction for the av6z calculation had the effect of decreasing the depth of the potential by approximately 10% (this was observed for both linear and non-linear geometries). As the BSSE corrected potentials generally underestimate the well depths for this type of complex by more than 10%, the additional computational effort of applying the correction was judged to be unwarranted.

The prediction of a linear equilibrium structure for NH(X)–Ne was surprising, given that high-level calculations for NH(X)–He and NH(X)–Ar yielded bent equilibrium structures.<sup>8,10–12</sup> However, the potential energy surface for NH(X)–Ne was found to be quite weakly anisotropic. At the CASPT2/av6z level bending the complex from  $\theta = 0$  to  $60^\circ$  increased the potential energy by just  $7 \text{ cm}^{-1}$ . Hence the bond angle could be very sensitive to small errors. To further investigate the equilibrium structure of the ground state we performed RCCSD(T) calculations with the basis sets described above and with basis sets that included mid-bond functions.<sup>27</sup> The latter consisted of

**Table 1** Band origins, rotational constants and assignments for the A  $^3\Pi$ –X  $^3\Sigma^-$  bands of NH/D–Ne

NH–Ne				ND–Ne		
$P'^a$	0–0 <sup>b</sup>	1–0 <sup>b</sup>	$B'^c$	0–0 <sup>b</sup>	1–0 <sup>b</sup>	$B'^c$
2 <sub>1</sub>	29 758.7(1)	32 791.7(1)	0.146	<sup>d</sup>	32 023.1(1)	0.151
1 <sub>1</sub>	29 767.5(1)	32 800.8(1)	0.149			
2 <sub>u</sub>	29 771.9(1)		0.149			
1 <sub>u</sub>	29 772.8(1)	32 805.7	0.147			
$^3\Pi_1, 0^-$	29 798.6(1)	32 831.5(1)	0.159	29 809.2(1)	32 066.2(1)	0.163
$^3\Pi_1, 0^+$	29 812.2(5)	32 845.0(5)	<sup>e</sup>	29 822.8(5)	32 078.3(5)	<sup>e</sup>
$^3\Pi_0, 0^-$	29 830.8(5)	32 863.9(5)	<sup>e</sup>	29841(1)	32098(1)	<sup>e</sup>

Ground state rotational constants

NH(X)–Ne,  $B'' = 0.149(2)$

ND(X)–Ne,  $B'' = 0.151(2)$

<sup>a</sup> Assignments are for  $^3\Pi_2$  unless otherwise indicated. <sup>b</sup> NH/D vibrational quantum numbers for the upper and lower states. Energies are given in  $\text{cm}^{-1}$  units with  $1 - \sigma$  errors for the last digit in parentheses. <sup>c</sup> Rotational constants in  $\text{cm}^{-1}$  units. Constants for the  $v' = 0$  and  $v' = 1$  bands were indistinguishable, within the experimental errors. The  $1 - \sigma$  errors in the rotational constants were  $\pm 0.003 \text{ cm}^{-1}$ . <sup>d</sup> The density of monomer lines precluded the assignment of many of the ND–Ne bands. <sup>e</sup> Diffuse band that did not exhibit rotational structure.

**Table 2** Comparison of calculated bond energies and equilibrium distances<sup>a</sup> using different correlation methods and basis sets

Basis <sup>b</sup> /method	$D_e/\text{cm}^{-1}$ (uncorrected)				$D_e/\text{cm}^{-1}$ (CP corrected)				
	CASPT2	CASPT3	MRCI <sup>c</sup>	RCCSD(T)	CASPT2	CASPT3	MRCI <sup>c</sup>	RCCSD(T)	RCCSD(T)-BF <sup>d</sup>
X-state									
avdz	-84.15	-53.30	-53.31	-68.8 <sup>e</sup>	-17.41	-16.43	-13.47	-20.0 <sup>e</sup>	-39.1
avtz	-88.79	-68.72	-56.85	-57.3	-33.36	-26.91	-20.95	-33.3	-40.5
avqz	-108.9	-54.23	-43.57	-50.8	-31.94	-27.04	-21.40	-37.1	-41.6
av5z	-43.25	-35.98	-28.00	-43.2	-32.11	-27.81	-21.62	-38.6	-42.2
av6z	-42.44	-31.67	—	-41.6	-37.94	-28.20	—	-39.1	-42.3
A-state									
avdz	-157.5	-105.4	-104.5	—	-48.42	-50.00	-44.60	—	—
avtz	-189.3	-145.9	-123.1	—	-80.92	-64.60	-51.45	—	—
avqz	-186.7	-107.5	-92.57	—	-84.25	-65.63	-54.14	—	—
av5z	-97.26	-81.25	-66.96	—	-78.75	-68.99	-55.72	—	—
av6z	-95.13	-76.53	—	—	-86.06	-71.32	—	—	—

Basis <sup>b</sup> /method	$R_e/\text{bohr}$ (uncorrected)				$R_e/\text{bohr}$ (CP corrected)				
	CASPT2	CASPT3	MRCI <sup>c</sup>	RCCSD(T)	CASPT2	CASPT3	MRCI <sup>c</sup>	RCCSD(T)	RCCSD(T)-BF
X-state									
avdz	7.14	7.30	7.30	6.86 <sup>e</sup>	6.86	7.61	7.75	7.54 <sup>e</sup>	6.53
avtz	6.77	6.78	6.84	6.38	6.66	7.30	7.56	6.58	6.48
avqz	6.82	6.88	7.00	6.40	7.22	7.30	7.53	6.55	6.46
av5z	7.24	7.15	7.33	6.45	7.39	7.27	7.44	6.50	6.46
av6z	7.30	7.19	—	6.48	7.36	7.24	—	6.52	6.46
A-state									
avdz	6.21	6.50	6.51	—	6.63	6.63	6.72	—	—
avtz	5.93	6.05	6.12	—	6.46	6.57	6.50	—	—
avqz	6.15	6.35	6.44	—	6.46	6.50	6.67	—	—
av5z	6.41	6.51	6.51	—	6.48	6.52	6.59	—	—
av6z	6.41	6.44	—	—	6.46	6.51	—	—	—

<sup>a</sup> The minima represent the global minimum ( $\theta = 0^\circ$ ) in which NH–Ne is linear for both the X and A states for the CASPT2, CASPT3 and MRCI methods, whereas for the RCCSD(T) method the global minimum is closer to  $\theta = 60^\circ$  for the X-state. <sup>b</sup> Basis set truncated using spdf functions on N and Ne, and spd functions on H. <sup>c</sup> Davidson corrected energies. <sup>d</sup> Calculation with spdf bond functions (BF) centered at the midpoint of Ne to the center of mass of NH bond distance. <sup>e</sup> For the avdz basis set the global minima is at  $\theta = 0^\circ$  for the X-state calculated *via* RCCSD(T).

3s, 3p, 2d and 1f functions with the exponents 0.9, 0.3, 0.1 for the s and p functions, 0.2 for d and 0.3 for f. Application of the BSSE correction was found to be essential when the mid-bond functions were used. Results from the CCSD(T) calculations are collected in Table 2. For all basis sets larger than avdz the equilibrium bond angle was found to be near  $60^\circ$ . The ground state potential energy surface was characterized using the highest level of theory (RCCSD(T)/av6z with mid-bond functions and BSSE corrections).

Potential energy points for the X and A states were calculated on a Jacobi grid that consisted of 13 radial positions ( $R = 5.0$  to  $9.0$  in steps of  $0.5$ , plus  $10$ ,  $12$ ,  $14$  and  $20$  au) and 7 angles ( $\theta = 0$  to  $180^\circ$  in steps of  $30^\circ$ ). A contour plot of the potential energy surface for NH(X)–Ne is shown in Fig. 6. This surface is weakly anisotropic with a single minimum for the bent structure ( $D_e'' = 42.3 \text{ cm}^{-1}$ ,  $\theta_e'' = 63.7^\circ$ ,  $R_e'' = 6.46 \text{ au}$ ). The barrier to NH rotation along the minimum energy path is only  $9 \text{ cm}^{-1}$ , which is smaller than the diatomic rotational constant ( $B_0'' = 16.34 \text{ cm}^{-1}$ ).

Potential energy surfaces for the A state are shown in Fig. 7. The global minimum is for the linear hydrogen-bonded configuration ( $D_e' = 95 \text{ cm}^{-1}$ ,  $R_e' = 6.41 \text{ au}$ ) but there is a secondary minimum for the alternative linear configuration ( $E_{\text{min}} = 47 \text{ cm}^{-1}$ ,  $R_{\text{min}} = 6.00 \text{ au}$ ). From Fig. 7 it is apparent that the difference potential for the A state (defined by  $V_{\text{diff}} = (-1)^{\Lambda}(V_{A'} - V_{A''})/2$ ) is appreciable. The barriers to NH rotation (relative to the global minimum) are  $62$  and  $78 \text{ cm}^{-1}$  on the A' and A'' surfaces, respectively.

To facilitate calculation of the bound ro-vibrational levels of the X and A states, and to provide a convenient way of

reporting the potential energy surfaces, each series of energy points for a fixed value of the Jacobi angle ( $\theta_i$ ) were fit to the

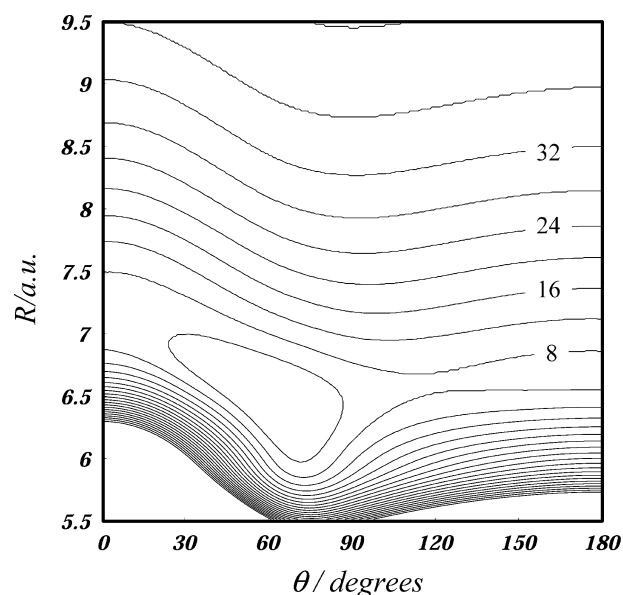


**Fig. 6** Contour plot of the potential energy surface for NH(X  $^3\Sigma^-$ )–Ne. The linear NH–Ne geometry corresponds to  $\theta = 0^\circ$ . The contours are drawn from the global minimum at  $-42 \text{ cm}^{-1}$  with  $4 \text{ cm}^{-1}$  intervals. The numbers on the contour lines give the energy (in  $\text{cm}^{-1}$ ) above the global minimum.

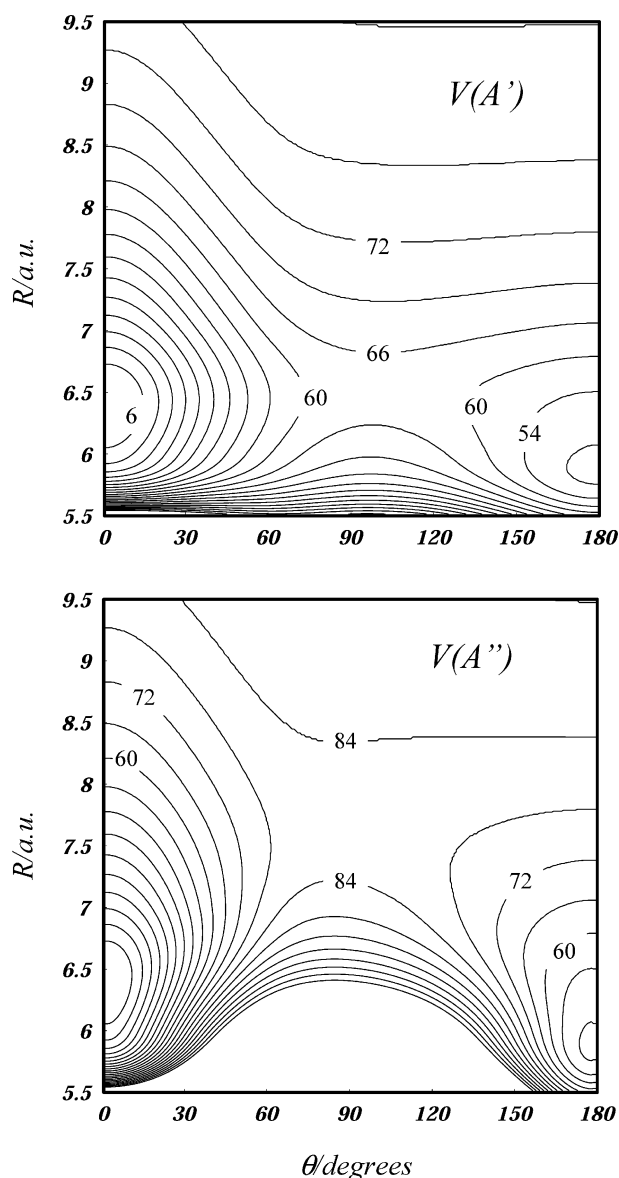


**Fig. 7** Contour plots of the potential energy surfaces for NH(A  $^3\Pi$ )-Ne. The upper and lower panels show the A' and A'' surfaces, respectively. The linear NH-Ne geometry corresponds to  $\theta = 0^\circ$ . The contours are drawn from the linear NH-Ne geometry contour at  $-94 \text{ cm}^{-1}$  with  $6 \text{ cm}^{-1}$  intervals. The numbers on the contour lines give the energy (in  $\text{cm}^{-1}$ ) above the global minimum.

radial function<sup>16</sup>

$$V(R, \theta_i) = c_{1i} \exp(-b_{1i}R) + (c_{2i} + c_{3i}R) \exp(-b_{2i}R) + c_{4i} \{ \tanh[1.2(R - R_{0i})] + 1 \} / R^6 \quad (1)$$

Fitting was accomplished using a standard non-linear least-squares fitting routine (Levenberg-Marquardt). The values of the fitting parameters obtained for the X and A state surfaces

**Table 3** Fitting parameters for NH(X)-Ne potential energy surfaces<sup>a</sup>

	0°	30°	60°	90°	120°	150°	180°
$b_1$	0.817 929	0.797 212	0.770 407	0.757 023	0.757 222	0.760 312	0.759 758
$b_2$	2.430 871	2.500 130	2.709 410	2.689 872	2.607 936	2.568 975	2.562 518
$R_0$	10.297 800	10.268 210	10.263 560	10.335 650	10.351 200	10.361 060	10.347 730
$c_1$	-2.0690 17(+4)	-1.452 899(+4)	-8.525 777(+3)	-6.817 797(+3)	-7.257 000(+3)	-8.091 673(+3)	-8.316 639(+3)
$c_2$	-3.729 794(+8)	-3.904 316(+8)	-5.779 563(+8)	-4.209 379(+8)	-3.389 168(+8)	-3.076 226(+8)	-3.126 880(+8)
$c_3$	1.620 229(+8)	1.501 971(+8)	1.902 710(+8)	1.392 180(+8)	1.169 704(+8)	1.123 698(+8)	1.159 008(+8)
$c_4$	-1.250 320(+6)	-1.050 519(+6)	-8.547 407(+5)	-7.716 812(+5)	-7.960 255(+5)	-9.106 453(+5)	-8.882 603(+5)

<sup>a</sup> Parameters for eqn. (1). Exponents are given in parentheses. The energies are in  $\text{cm}^{-1}$  and the distances in au.

are listed in Tables 3 and 4, respectively. For the X-state the difference between the energy points and the fitted potential was no greater than  $0.2 \text{ cm}^{-1}$ , and the rms deviation was  $0.07 \text{ cm}^{-1}$ . Similarly, for the A-state surfaces the largest deviation was  $0.24 \text{ cm}^{-1}$ , with an rms error of  $0.07 \text{ cm}^{-1}$ .

### Calculation of the bound states of NH/D(X,A)-Ne

The bound states supported by the NH-Ne X and A state interaction potentials were obtained by finding the eigenvalues of the model Hamiltonian defined by

$$\hat{H} = \hat{h}_{\text{diatom}} - \frac{\hbar^2}{2\mu R} \frac{\partial^2}{\partial R^2} R + \frac{\hat{L}^2}{2\mu R^2} + V(R, \theta) \quad (2)$$

where  $\hat{h}_{\text{diatom}}$  is the effective Hamiltonian for the diatom,  $\mu$  is the NH-Ne reduced mass and  $\hat{L}$  is the angular momentum operator for end-over-end rotation of the complex.  $V(R, \theta)$  represents the interaction potential. It was assumed that the high frequency vibration of N-H could be adiabatically uncoupled from the low-frequency intermolecular motions. The diatomic Hamiltonian for the  $^3\Sigma^-$  state was defined by<sup>8</sup>

$$\hat{h}_{\text{diatom}} = b_{\text{NH}}^X \hat{n}^2 + \frac{2}{3} \lambda_0^X (3s_\zeta^2 - s^2) + \gamma_0 \hat{n} \hat{s} \quad (3)$$

where  $s_\zeta$  is the projection of the spin on the diatomic axis. The diatomic constants are (in  $\text{cm}^{-1}$  units)  $b_{\text{NH}}^X = 16.343$  (rotational constant),  $\lambda_0^X = 0.920$  (spin-spin coupling), and  $\gamma_0 = -0.055$  (spin-rotation coupling).<sup>22</sup> As only the zero-point level was observed for the ground state, the bound states of ND(X)-Ne were not calculated. The effective Hamiltonian for the A  $^3\Pi$  state was given by<sup>18</sup>

$$\hat{h}_{\text{diatom}} = b_{\text{NH}}^A (j^2 + s^2 - j_\zeta^2 - s_\zeta^2 - j_- \hat{s}_- - j_+ \hat{s}_+) + a l_\zeta \hat{s}_\zeta + \frac{2}{3} \lambda_0^A (3s_\zeta^2 - s^2) \quad (4)$$

where  $l_\zeta$  and  $j_\zeta$  are the projections of the orbital and total angular momentum on the diatomic axis. The molecular constants for  $v = 0$  are  $b_{\text{NH}}^A = 16.32$  [8.79],  $A = -34.62$  [-34.58], and  $\lambda_0^A = -0.199$  68, where the values in square brackets are for ND.<sup>23</sup>

The eigenvalues and eigenfunctions for the bound states of NH(A,X)-Ne were determined variationally. Calculations for NH-Ne in both the X and A states were carried out using computer codes developed by Groenenboom *et al.*<sup>28</sup> For the diatom, Hund's case 'a' and 'b' basis functions were used for the A and X states, respectively.

### Comparison of theoretical and experimental results for NH(X)-Ne

Calculated energies for NH(X)-Ne are presented in Table 5. These are relative to the NH(X,  $n = 0, j = 1$ ) + Ne dissociation asymptote. The energy level structure is well approximated by the expression

$$E(v, L) = T_v'' + B_v'' L(L + 1) \quad (5)$$

**Table 4** Fitting parameters for NH(A)–Ne potential energy surfaces<sup>a</sup>

	0°	30°	60°	90°	120°	150°	180°
$b_1$	0.676 965 0.676 965	0.713 237 0.660 234	0.705 047 0.607 847	0.702 418 0.603 522	0.716 062 0.576 116	0.729 579 0.640 584	0.744 456 0.744 456
$b_2$	3.225 655 3.225 655	2.889 252 2.590 730	2.881 204 2.297 620	2.772 838 2.246 454	2.847 700 2.509 841	3.014 996 2.664 735	3.115 852 3.115 852
$R_0$	10.846 251 10.846 251	9.287 879 10.634 214	10.392 242 6.756 457	10.503 540 6.789 849	10.397 723 6.727 464	10.376 575 6.107 604	10.311 696 10.311 696
$c_1$	−9.079 756(+3) −9.079 756(+3)	−8.852 722(+3) −5.674 334(+3)	−5.003 136(+3) −1.952 041(+3)	−4.029 205(+3) −1.609 412(+3)	−4.415 425(+3) −1.071 379(+3)	−5.005 365(+3) −2.098 065(+3)	−5.724 223(+3) −5.724 223(+3)
$c_2$	−3.156 970(+10) −3.156 970(+10)	−2.554 330(+9) −4.167 856(+8)	−1.568 878(+9) −7.883 147(+7)	−6.828 686(+8) −6.461 857(+7)	−1.129 075(+9) −3.820 124(+8)	−2.547 804(+9) −3.345 586(+8)	−3.840 986(+9) −3.840 986(+9)
$c_3$	8.216 246(+9) 8.216 246(+9)	7.735 767(+8) 1.590 394(+8)	4.629 448(+8) 3.404 260(+7)	2.118 631(+8) 2.784 669(+7)	3.303 165(+8) 1.201 001(+8)	7.054 208(+8) 1.162 654(+8)	1.042 055(+9) 1.042 055(+9)
$c_4$	−4.439 048(+5) −4.439 048(+5)	−5.178 024(+5) −4.378 473(+5)	−7.303 060(+5) −2.876 895(+5)	−6.947 215(+5) −3.363 799(+5)	−7.638 865(+5) −5.389 964(+5)	−8.412 363(+5) −2.931 007(+5)	−9.392 387(+5) −9.392 387(+5)

<sup>a</sup> Parameters for eqn. (1). The upper and lower entries are for the A' and A'' states, respectively. Exponents are given in parentheses. The energies are in cm<sup>−1</sup> and the distances in au.

where  $T_v''$  the vibrational energy for the non-rotating complex and  $B_v''$  is the effective rotational constant for end-over-end rotation. The electron spin is weakly coupled to the rotational motion, such that there are three closely spaced levels for all states with  $L > 0$ . In Table 5 we organize the states according to the relationship between  $J$  and  $L$ ;  $J = L + 1$ ,  $J = L$  and  $J = L - 1$ . The  $J = L \pm 1$  levels are of e-symmetry while the  $J = L$  levels have f-symmetry. The last column in Table 5 lists  $B_v''$  constants calculated from  $\langle R^{-2} \rangle$  expectation values. Constants for the  $J = L - 1$  manifold are shown. The constants from  $\langle R^{-2} \rangle$  were in good agreement with those obtained by fitting eqn. (5) to the energy levels.

The potential for NH(X)–Ne supports one bound vibrationally excited level for the –Ne stretch. The stretch states were easily recognized as they exhibit significantly smaller rotational constants. Excited bending levels of the complex were not predicted to be stable. NH(X) performs nearly free rotation within the complex, so the excited bending levels are associated with  $n = 1$ , which lies approximately 32.6 cm<sup>−1</sup> above  $n = 0$  for the diatom. The attractive component of the interaction between NH(X,  $n = 1$ ) and Ne is not sufficiently strong to bring the associated states of the complex down below the NH(X,  $n = 0$ ) + Ne asymptote.

Calculated properties for NH(X)–Ne were in agreement with the experimental observations. The rotational structure of the A–X transitions did not show resolvable spin-splittings for the lower state, consistent with the predicted weakness of the spin-rotation coupling. Theory yielded a zero-point level that was

**Table 5** Calculated energy levels and effective rotational constants for NH(X)–Ne<sup>a</sup>

$L$	$v_s^b$	$J = L + 1$	$J = L$	$J = L - 1$	$B^c$
0	0	−23.50			
1	0	−23.21	−23.21	−23.20	0.1473
2	0		−22.62	−22.61	0.1471
3				−21.73	0.1468
0	1	−6.63			
1	1	−6.41	−6.41	−6.41	0.1093
2	1		−5.97	−5.97	0.1086
3	1			−5.32	0.1076

<sup>a</sup> Energies and rotational constant in cm<sup>−1</sup> units. The energies are defined relative to the NH(X,  $n = 0$ ,  $j = 1$ ) + Ne dissociation asymptote. <sup>b</sup> Vibrational quantum number for the NH–Ne stretch. <sup>c</sup> Rotational constants derived from  $\langle R^{-2} \rangle$  expectation values for the  $J = L - 1$  component.

relatively well separated from the excited vibrational level ( $\Delta G_{1/2} = 16.9$  cm<sup>−1</sup>) so that a spectrum recorded under low temperature conditions would be dominated by transitions from a single lower level. The observed bands were consistent with this expectation. The theoretical value for  $D_0''$  of 23.50 cm<sup>−1</sup> (cf. Table 5) is within the experimental range, while the calculated rotational constant of 0.147 cm<sup>−1</sup> is at the edge for the  $1 - \sigma$  error range for the observed value of 0.149(2) cm<sup>−1</sup>.

### Comparison of theoretical and experimental results for NH/D(A)–Ne

Calculations for NH(A)–Ne predict that all of the observed states associated with the NH(A <sup>3</sup>Π<sub>2</sub>,  $j = 2$ ) + Ne asymptote are stable. The most deeply bound state yields a dissociation energy of  $D_0'' = 30.6$  cm<sup>−1</sup>, well within the experimental range. States correlating with NH(A <sup>3</sup>Π<sub>1</sub>,  $j = 1$ ) and NH(A <sup>3</sup>Π<sub>0</sub>,  $j = 0$ ) are above the lowest energy dissociation asymptote. The states that correlate with NH(A <sup>3</sup>Π<sub>3</sub>,  $j = 3$ ) are even higher in energy. Adiabatic bender potentials<sup>16,17,29</sup> for NH(A)–Ne provide a useful means for understanding the pattern of vibronic energy levels. These curves were constructed by diagonalizing the Hamiltonian matrix at a series of fixed values for  $R$ . The adiabatic bender potential curves are shown in Fig. 8. The interaction between NH(A <sup>3</sup>Π<sub>2</sub>) and Ne splits the  $j = 2$  level into five states of + parity and five states of − parity. For  $P > 0$  these ± levels occur in nearly degenerate pairs while the  $P = 0^+$  and  $0^-$  states are well separated. In the following we differentiate  $P > 0$  states that have the same values for  $P$  and  $j$  by adding the u/l subscript to indicate the upper/lower energy member of the pair. Hence Fig. 8 shows (in ascending energy order) the  $P = 2_l, 1_l, 2_u, 1_u, 0^+$  levels for the + parity states (upper panel) and the  $P = 2_l, 1_l, 0^-, 2_u, 1_u$  levels for the − parity states (lower panel). The nearly degenerate ± parity doublets for  $P > 0$  levels are treated as components of one state in comparing the predicted energy levels with the observed spectrum.

In Fig. 8 it is apparent that the 2<sub>l</sub> state supports the lowest energy vibronic level and that the excited bending levels are clustered together in an energy band that spans approximately 10 cm<sup>−1</sup>. The NH(A <sup>3</sup>Π<sub>1</sub>,  $j = 1$ ) state is split into  $P = 0^-, 1_l, 0^+$  and 1<sub>u</sub> states by the interaction with Ne (where the  $P = 1$  levels are parity doublets). Of this group, only the  $P = 0^-$  state exhibited resolvable rotational structure in our experiments. Lastly, a pair of  $P = 0^+$  and  $0^-$  states correlate with NH(A <sup>3</sup>Π<sub>0</sub>,  $j = 0$ )–Ne.

Accurate energies for the bound states supported by the *ab initio* potential are presented in Table 6, which includes rotational constants obtained from  $\langle R^{-2} \rangle$  values. In comparing

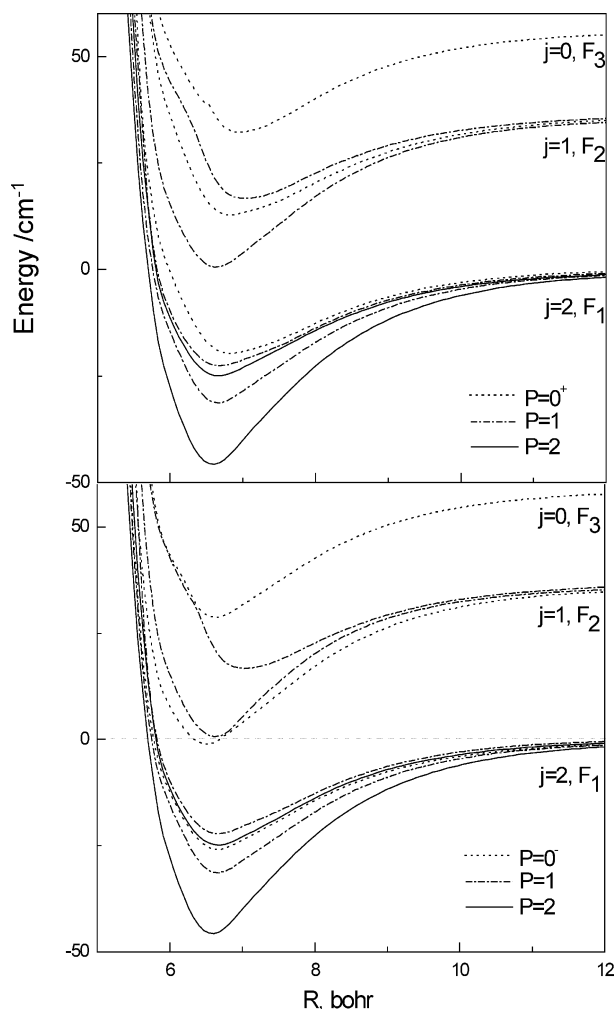


**Fig. 8** Adiabatic bender potentials for NH(A)–Ne. The upper and lower panels show states of + and – parity, respectively. These curves were calculated for total angular momentum  $J = 2$ . The dissociation asymptotes are labeled by the NH angular momentum ( $j$ ) and the spin-orbit component. In the case ‘a’ limit  $F_1 = {}^3\Pi_2$ ,  $F_2 = {}^3\Pi_1$  and  $F_3 = {}^3\Pi_0$ .

the theoretical predictions with the experimental observations we begin by noting that the rotational constants for the

**Table 6** Calculated energy levels and rotational constants for NH (A  ${}^3\Pi_2$ ,  $\nu = 0$ )–Ne for  $J = 2^a$

$P$	$\nu_s$	ABE <sup>b</sup>	$p = 1^c$	$p = -1$	$B^d$
2 <sub>1</sub>	0	-30.81	-30.64	-30.64	0.1499
1 <sub>1</sub>	0	-19.87	-19.35	-19.2	0.1424
0 <sup>-</sup>	0	-15.76	-15.41		0.1406
2 <sub>u</sub>	0	-14.81	-15.06	-15.13	0.1403
1 <sub>u</sub>	0	-12.85	-12.63	-13.19	0.1372
0 <sup>+</sup>	0	-11.33		-11.21	0.1289
2 <sub>1</sub>	1	-11.35	-10.98	-10.97	0.1168
1 <sub>1</sub>	1	-5.82	-5.44	-5.31	0.1044
0 <sup>-</sup>	1	-3.85	-3.64		0.0982
2 <sub>u</sub>	1	-3.09	-3.33	-3.58	0.0976
1 <sub>u</sub>	1	-2.24	-2.28	-2.78	0.0943
0 <sup>+</sup>	1	-1.57		-1.63	0.087

<sup>a</sup> Energies and rotational constant in  $\text{cm}^{-1}$  units. The energies are defined relative to the NH(A  ${}^3\Pi_2$ ,  $j = 2$ ) + Ne dissociation asymptote. <sup>b</sup> Energies calculated from the adiabatic bender curves for  $J = 2$ . The minus parity curves were used for all states with the exception of 0<sup>+</sup>. <sup>c</sup> Spectroscopic parity. <sup>d</sup> The rotational constants were calculated from  $\langle R^{-2} \rangle$  expectation values for the  $p = 1$  component, with the exception of the  $P = 0^+$  state.

**Table 7** Comparison of calculated and measured spectroscopic properties for NH(A  ${}^3\Pi$ ,  $\nu = 0$ )–Ne<sup>a</sup>

$P^b$	$E(p = 1)_{\text{calc}}^c$	$E(p = -1)_{\text{calc}}^c$	$E_{\text{obs}}$	$B_{\text{calc}}^d$	$B_{\text{obs}}^e$
2 <sub>1</sub>	0.00	0.00	0.0	0.1499	0.146
1 <sub>1</sub>	11.29	11.44	9.6	0.1424	0.149
0 <sup>-</sup>	15.23	—	—	0.1406	—
2 <sub>u</sub>	15.58	15.50	13.7	0.1403	0.149
1 <sub>u</sub>	18.01	17.45	14.6	0.1372	0.147
0 <sup>+</sup>	—	19.43	—	0.1289	—
${}^3\Pi_1$ , 0 <sup>-</sup>	—	41.2	40.4	0.1526	0.159
${}^3\Pi_1$ , 0 <sup>+</sup>	56.2	—	54.7	—	diffuse
${}^3\Pi_0$ , 0 <sup>-</sup>	71.1	—	72.8	—	diffuse

<sup>a</sup> Relative energies and rotational constants in units of  $\text{cm}^{-1}$ . <sup>b</sup> Assignments are for  ${}^3\Pi_2$  unless otherwise indicated. <sup>c</sup> Energies below  $29 \text{ cm}^{-1}$  are from variational calculations for  $J = 2$ . Energies above  $29 \text{ cm}^{-1}$  were obtained from the zero-point levels of the adiabatic bend potentials. <sup>d</sup> The rotational constants were calculated from  $\langle R^{-2} \rangle$  expectation values. <sup>e</sup> Error limits are  $\pm 0.003$ .

assigned bands of NH/D–Ne did not show any marked decrease with increasing excitation energy. This implies that the NH/D–Ne stretch vibration was not being excited ( $\nu_s = 0$ ). For example, the calculations predict that the rotational constant for the  $P' = 2_1$  state will decrease by 18% when the –Ne stretch is excited (*cf.* Table 6). Conversely, the highest energy band of NH/D–Ne with resolvable structure had the largest rotational constant. Calculations were performed for NH/D(A,  $\nu = 0$ )–Ne so that the relevant comparison is with the data for the complex bands associated with the monomer 0–0 transition. However, as the NH/D(A)–Ne interaction was imperceptibly influenced by NH/D vibrational excitation, the assignments derived for the 0–0 band data were readily transferred to the complex features associated with the monomer 1–0 transition.

Overall, the agreement between the observed and calculated energy level structure for NH(A,  $\nu = 0$ )–Ne was satisfactory. Measured and calculated level spacings and rotational constants are collected for comparison in Table 7. At the semi-quantitative level the predicted energy ordering of the  $P$ -states was consistent with the observations. The calculated rotational constants were in reasonable agreement with experiment for the lower energy  $P$ -states. The calculations for the  $j = 2$ ,  $P' = 2_u$  and  $1_u$  levels appear to give underestimates for the rotational constants, but this is due to the circumstance that the constants were calculated from  $\langle R^{-2} \rangle$  expectation values, and therefore do not include the effects of Coriolis coupling. The splittings between the various  $P'$ -states of  ${}^3\Pi_2$ ,  $j = 2$  are overestimated by the calculations, which indicates that the anisotropies of the *ab initio* potential energy surfaces for the A-state are too great. However, as noted above, the well depth is compatible with the spectroscopic data. Combining the calculations for the A and X states yields a value for the red-shift of the complex origin band, relative to the monomer, of  $7.1 \text{ cm}^{-1}$  as compared to the measured value of  $12.4 \text{ cm}^{-1}$ .

The energies for predissociated states of NH(A)–Ne were located by finding the vibrational eigenvalues for the adiabatic bender curves. As a test of the reliability of this approximation, the zero-point energies for the adiabatic bender potentials for the  $\omega = 2$ ,  $j = 2$  states were calculated for comparison with the full close coupling calculations. The results, given in Table 6, indicate that adiabatic bender potentials yield zero-point energies that are in error by less than  $0.6 \text{ cm}^{-1}$ . The adiabatic bender potentials (Fig. 8) locate the zero-point level for  ${}^3\Pi_1$ ,  $j = 1$ ,  $P' = 0^-$  at  $41.2 \text{ cm}^{-1}$  above  $P' = 2_1$ , close to the measured interval of  $40.4 \text{ cm}^{-1}$ . These calculations also provide reasonable assignments for the prominent diffuse features observed on the high frequency side of the monomer Q<sub>21</sub>(1) and P<sub>31</sub>(1) lines. These are attributed to  ${}^3\Pi_1$ ,  $P' = 0^+$  and  ${}^3\Pi_0$ ,  $P' = 0^+/0^-$ , respectively.

## Discussion

As in our recent work on the  $c$ - $a$  transition of  $\text{NH-Ne}$ ,<sup>17</sup> we find that high-level theoretical calculations are sufficiently accurate to guide the assignment of the  $A$ - $X$  spectrum. It is of interest to compare the results for the  $c$ - $a$  and  $A$ - $X$  transitions as they arise from common electronic configurations. The lower states,  $X$  and  $a$ , are derived from  $(1\sigma)^2(2\sigma)^2(3\sigma)^2(1\pi)^2$  while the upper states,  $A$  and  $c$  are from  $(1\sigma)^2(2\sigma)^2(3\sigma)(1\pi)^3$ . Dispersion and repulsive exchange forces dominate the  $\text{NH-Ne}$  interactions, so it was anticipated that the potential energy surfaces for states of  $\text{NH}$  derived from a common configuration would be quite similar. The *ab initio* calculations confirm this expectation. The CASPT2/av6z potential energy surfaces for the  $X$  and  $a$  states have linear minima with well depths of ( $D_e$ ) of  $42\text{ cm}^{-1}$  ( $X$ ) and  $43\text{ cm}^{-1}$  ( $A$ ). The  $R_e$  values are also similar ( $7.30$  vs.  $7.41$  au). With the larger basis sets RCCSD(T) calculations for  $\text{NH}(X)\text{-Ne}$  yielded a bent equilibrium geometry and it is quite possible that the anisotropy of the  $A$ -state would change in going from CASPT2 to RCCSD(T). The observed rotational constant for  $\text{NH}(a)\text{-Ne}$  was not reproduced by ro-vibrational energy level calculations that used the CASPT2/av6z potential energy surface. It was noted that this error might stem from overestimation of the anisotropy of the potential. The present results for the ground state suggest that RSCCD(T) calculations for  $\text{NH}(a)\text{-Ne}$  may provide less anisotropic potential energy surfaces that yield better agreement with the experimental observations.

Potential energy surfaces for the  $A$  and  $c$  states of  $\text{NH-Ne}$  were similar in all respects (and consistent with calculations for the  $\text{He}$  and  $\text{Ar}$  complexes). The equilibrium structures are linear  $\text{NH-Ne}$  with  $D_e$  values of  $95\text{ cm}^{-1}$  ( $A$ ) and  $97\text{ cm}^{-1}$  ( $c$ ) and equilibrium distances of  $6.41$  and  $6.46$  au. Both states have secondary linear minima and for non-linear geometries the  $A'$  surfaces are less repulsive than the  $A''$  surfaces. Comparisons with the experimental data indicate that the  $A$ -state surfaces yield reasonable values for  $D_0$  and the rotational constants. The primary shortcoming is that the anisotropy of the surface is too great. The comparison for the  $c$  state is less satisfactory and somewhat puzzling. The  $c$  state surfaces appear to be too shallow (by a factor of approximately 1.4) while the rotational constants indicate the surfaces need to be translated further out along the  $R$ -axis (by about  $0.4$  au). The reasons for these discrepancies have yet to be identified. In future studies it will be of interest to see if higher level calculations (such as RCCSD(T)) for the electronically excited states can provide significantly better accuracy.

## Acknowledgements

Support of this work by the National Science Foundation under grant CHE-0213313 is gratefully acknowledged.

## References

- 1 A. Kaes and F. Stuhl, *J. Chem. Phys.*, 1992, **97**(7), 4661.

- 2 (a) L. Neitsch, F. Stuhl, P. J. Dagdigian and M. H. Alexander, *J. Chem. Phys.*, 1996, **104**, 1325; (b) P. S. Zuchowski, B. Bussery-Honvault, R. Moszynski and B. Jeziorski, *J. Chem. Phys.*, 2003, **119**(20), 10497.
- 3 M. H. Alexander, P. J. Dagdigian and D. Lemoine, *J. Chem. Phys.*, 1991, **95**, 5036.
- 4 J. L. Rinnenthal and K.-H. Gericke, *J. Chem. Phys.*, 2000, **113**, 6210.
- 5 J. L. Rinnenthal and K.-H. Gericke, *J. Chem. Phys.*, 2002, **116**, 9776.
- 6 P. J. Dagdigian, *J. Chem. Phys.*, 1989, **90**, 6110.
- 7 G. Kerenskaya, U. Schnupf, M. C. Heaven and A. van der Avoird, *J. Chem. Phys.*, 2004, **121**, 7549.
- 8 H. Cybulski, R. V. Krems, H. R. Sadeghpour, A. Dalgarno, J. Klos, G. C. Groenenboom, A. van der Avoird, D. Zgid and G. Chalasinski, *J. Chem. Phys.*, in press.
- 9 R. Jonas and V. Steamlmer, *Z. Phys. D: At., Mol. Clusters*, 1989, **14**, 143.
- 10 R. V. Krems, H. R. Sadeghpour, A. Dalgarno, D. Zgid, J. Klos and G. Chalasinski, *Phys. Rev. A: At., Mol., Opt. Phys.*, 2003, **68**, 51401/1.
- 11 R. A. Kendall, G. Chalasinski, J. Klos, R. Bukowski, M. W. Severson, M. M. Szczesniak and S. M. Cybulski, *J. Chem. Phys.*, 1998, **108**, 3235.
- 12 G. Jansen and A. Hess, *Chem. Phys. Lett.*, 1992, **192**, 21.
- 13 L. Neitsch, F. Stuhl, P. J. Dagdigian and M. H. Alexander, *J. Chem. Phys.*, 1996, **104**, 1325.
- 14 S. Y. T. van de Meerakker, R. T. Jongma, H. L. Bethlem and G. Meijer, *Phys. Rev. A: At., Mol. Opt. Phys.*, 2001, **64**, 41401/1.
- 15 A. Kaes and F. Stuhl, *J. Chem. Phys.*, 1992, **97**, 7362.
- 16 M. Yang, M. H. Alexander, C.-C. Chang, R. W. Randall and M. I. Lester, *J. Chem. Phys.*, 1995, **103**, 905.
- 17 G. Kerenskaya, U. Schnupf and M. C. Heaven, *J. Chem. Phys.*, 2003, **119**, 8424.
- 18 W. B. Zeimen, G. C. Groenenboom and A. van der Avoird, *J. Chem. Phys.*, 2003, **119**, 131.
- 19 W. B. Zeimen, G. C. Groenenboom and A. van der Avoird, *J. Chem. Phys.*, 2003, **119**, 141.
- 20 M. H. Alexander, *Chem. Phys.*, 1985, **92**, 337.
- 21 M. C. Heaven, *Ann. Rev. Phys. Chem.*, 1992, **43**, 283.
- 22 C. R. Brazier, R. S. Ram and P. F. Bernath, *J. Mol. Spectrosc.*, 1986, **120**, 381.
- 23 P. Bollmark, I. Kopp and B. Rydh, *J. Mol. Spectrosc.*, 1970, **34**, 487.
- 24 M.-L. Dubernet, D. Flower and J. M. Hutson, *J. Chem. Phys.*, 1991, **94**, 7602.
- 25 (a) R. D. Amos, A. Bernhardsson, A. Berning, P. Celani, D. L. Cooper, M. J. O. Deegan, A. J. Dobbyn, F. Eckert, C. Hampel, G. Hetzer, P. J. Knowles, T. Korona, R. Lindh, A. W. Lloyd, S. J. McNicholas, F. R. Manby, W. Meyer, M. E. Mura, A. Nicklass, P. Palmieri, R. Pitzer, G. Rauhut, M. Schütz, U. Schumann, H. Stoll, A. J. Stone, R. Tarroni, T. Thorsteinsson and H.-J. Werner, *MOLPRO, a package of ab initio programs designed by H.-J. Werner and P. J. Knowles, Version 2002.1*, 2002; (b) The CASPT2 method used in these calculations is described in: H.-J. Werner, *Mol. Phys.*, 1996, **89**, 645.
- 26 (a) T. H. Dunning, *J. Phys. Chem.*, 2000, **104**, 9062; (b) R. A. Kendall, T. H. Dunning and R. J. Harrison, *J. Chem. Phys.*, 1992, **96**, 6796; (c) D. E. Woon and T. H. Dunning, *J. Chem. Phys.*, 1994, **100**, 2975.
- 27 (a) T. J. Giese and D. M. York, *Int. J. Quantum Chem.*, 2004, **98**, 388; (b) F. M. Tao, *THEOCHEM*, 1996, **367**, 55; (c) F.-M. Tao, *Int. Rev. Phys. Chem.*, 2001, **20**, 617.
- 28 G. C. Groenenboom and A. van der Avoird, unpublished computer codes.
- 29 M. H. Alexander, S. Gregurick, P. J. Dagdigian, G. W. Lemire, M. J. McQuaid and R. C. Sausa, *J. Chem. Phys.*, 1994, **101**, 4547.